Ultra-lightweight high ductility cement composite incorporated with low PE fiber and rubber powder

Zhenyu HUANG[a], Tingting LIANG[a], Bo HUANG[b], Yingwu ZHOU[a], Jianqiao YE[b]

[a] *Guangdong Provincial Key Laboratory of Durability for Marine Civil Engineering, Shenzhen University, Shenzhen 518060, China*

[b] *Department of Engineering, Lancaster University, Lancashire, LA1 4YW, UK*

Abstract

This paper presents the development and performance assessment of a novel ultra-lightweight high ductility cement composite (ULHDCC) incorporated with fly ash cenospheres, rubber powders and low fiber content of 0.7%. To address the brittle nature of such cement composite, this paper utilized the surface treated polyethylene (PE) fibers to improve the ductility behavior, and used rubber powders replacing part of cenospheres to reduce the matrix fracture toughness to achieve the pseudo-strain-hardening (PSH) performance. A fracture micromechanics-based investigation was performed to explain the high tensile ductility behavior of the ULHDCC. The mechanical properties including compressive and tensile strength, elastic modulus and microstructure has been experimentally examined. The results showed that the ULHDCC had the compressive strength ranging from 35.2MPa to 43.5MPa. The tensile strain in direct tensile test achieved 3% even with low fiber content of 0.7% PE fibers by volume. A relatively large amount of FAC (fly ash cenospheres) and rubber powder increased the entrapped air voids in the ULHDCC and reduced its density and strength. The ductility of ULHDCC was improved with the incorporation of rubber powder. Compared to normal engineering cement composite (ECC), to achieve similar tensile strain capacity the fiber content has been reduced 50% which leads to reduce the cost significantly.

Keywords: ECC; FAC; Fiber-reinforced; Lightweight concrete; High ductility

1. Introduction

Lightweight aggregate concrete (LWAC) has the characteristics of density less than 1950kg/m^3 and compressive strength between 10-35MPa [1]. LWAC can be used in industry and building structures to greatly reduce the self-weight, thereby reducing the amount of reinforcement in beams and columns, and the transportation, lifting and labor costs [2-6]. LWAC has been used in high-rise buildings, prefabricated structures, long-span bridges, offshore platform structures and other self-weight-sensitive structures [7-9]. Traditional lightweight aggregate concrete is made by using, e.g., expanded shale [10], expanded perlite [11], expanded polystyrene [12] and other natural or artificial materials. Although lightweight aggregate can reduce the density of concrete, the cylindrical compressive strength is normally low, which makes the compressive strength of concrete generally fail to meet the required structural design standard. This also leads to short-term construction, long-term shrinkage and deformation creep problems. To further lower the structural weight of offshore platform structures and improve the compressive strength of lightweight aggregate concrete, Chia et al. [13, 14] developed a new type of ultra-light cement composite material (ULCC) and applied it to the steel-concrete-steel composite structure [6, 9, 15-17]. The measured apparent density of ULCC is 1450kg/m^3 only, and its 28-day compressive strength can reach 60MPa, and its specific strength can reach 42.8kPa/(kg/m^3). The low density and high strength of ULCC was achieved by using cenospheres as fine aggregates. Cenospheres come from a by-product of coal-fired thermal power plants [18]. They have a thin hard shell on the outside and hollow interior filled with inert gas [19, 20]. Although the brittleness of ULCC limits its wider range of applications, its higher specific strength alone has obvious advantages. To reduce the brittleness of ULCC, it is feasible to mix fibers in the cement matrix [21].

Engineering cementitious composites (ECC) are fiber-reinforced cementitious composites with high tensile ductility. ECC were developed by Li in 1990s [22]. It was found that when the volume fraction of fiber does not exceed 2%, the tensile strain capacity of the ECC exceeds 3%, which is two orders of magnitude higher than that of ordinary concrete [22-25]. Table 1 shows the mechanical properties of different ECCs. Most ECCs are blended with 2% fibers to achieve a strain-hardened state and have high tensile ductility. ECCs overcome the inherent brittleness of concrete and exhibit a ductile failure mode. ECCs have a high tensile strain capacity developed by multiple micro-cracks, rather than a local and instantaneous fracture crack [26]. In previous studies, polyvinyl alcohol (PVA) [27, 28], polyethylene (PE) [29, 30] and polypropylene (PP) [31, 32] fibers have been added to cement matrix to bridge the growth of cracks, prevent the development of larger cracks and improve the tensile capacity of ECC. The downside of using EEC for large scale construction is the cost of fibers that exceeds three-quarters of the overall ECC cost [25, 33]. Thus, how to reduce fiber content while maintain high tensile strength of ECC has become a significant problem that demands urgent attention.

The number of rubber waste produced by waste tires increases with the rapid development of the automobile industry. Rubber may be grinded into smaller sizes and mixed with concrete as aggregates [34]. Adding rubber powder to replace fine aggregates can reduce density and improve ductility, toughness, impact resistance and thermal properties [35-37]. Adding rubber powder into ECC can reduce explosion spalling of ECC in fire [38], improve tensile strain capacity and crack resistance [39], improve ductility, reduce permeability [40], promote fiber dispersion and control matrix strength [27]. It is also recognized that adding rubber powder will considerably reduce the strength and stiffness of concrete. However, it has been found that graphene oxide can improve stiffness [41], and nano-silica [42] and high pozzolanic cementitious materials, such as silica fume and metakaolin, can reduce the negative impact on strength of concrete with rubber [43, 44]. Additionally, using rubber as aggregate is an effective method for recycling waste rubber and can reduce the cost of concrete and further decrease carbon footprint [45, 46].

In present study, a new cement composite material is developed by using rubber powders of different particle sizes to replace the cenospheres in ULCC with added PE fibers. By determining the mixing ratio, the research aims at achieving lightweight, high strength, high ductility and workable cement composite for various applications. The density, compressive and tensile strength, and tensile strain capacity of ULHDCC are studied experimentally at macroscopic level. Microscopic scale investigations using Mercury Intrusion Porosimetry (MIP) and Environmental Scanning Electron Microscopy (ESEM) are also carried out provide insights of the new material. On the basis of the micromechanics theory, matrix toughness and fiber/matrix interface properties of ULHDCC are then studied. Finally, the economic benefits of using the proposed mix ratio of this study are discussed, which provides an economic foundation for its application in a wider range of fields.

Table 1. Mechanical properties review of normal Engineering Cement Composites.

Literature	Fiber used	Strain capacity (%)	28-day Compressive Strength (MPa)	28-day Tensile Strength (MPa)	Density (kg/m^3)
Huang et al. [47]	0.7%PE fibers	3%-5%	24.9-43.5	3.5	1450
Yao et al. [30]	2%PE fibers	8.0%-11.14%	43-115	6.2-16.5	2136-2475
Yu et al. [48]	(0%-2.5%) PVA and (0%-2.5%) ST fibers	0.19%-5.48%	32.73-37.13	5.13-6.06	-
Wang et al. [33]	0%-2%PE and 2% steel fibers	0.37%-11.99%	36.4-48	4.54-8.19	2079.8-2236.8
Huang et al. [27]	2%PVA fibers	3.3%-4.4%	25.0-48.1	2.5-5.9	1649-1820
Yu et al. [29]	2%PE fibers	8.17%	112.69	17.42	2405
Deng et al. [49]	2% PVA fibers	1%	54.60	6.10	-
Chen et al. [50]	2%PVA fibers	1.5%-2.82%	63.94-75.58	3-5	1477.5-1962.2
Li et al. [51]	2% Fibers	1-8%	20-95	4-12	950-2300
Zhou et al. [52]	(0%-2%) PE fibers and (0-2%) ST fibers	2-9%	110.6-150.5	8.5-15.5	2474.4-2612

2. Materials and Concrete Mixing Method

2.1. Raw materials and mix proportion design

The raw materials of ULHDCC include ordinary Portland cement CEM I 52.5R, silica fume (SF), fly ash cenospheres (FAC), rubber powder and PE fibers. Figs. 1(a)-(c) shows the morphology of the raw material. The FAC was with a specific gravity of 870 kg/m^3, an average size of 20-300μm and a fineness modulus of 0.902 g/cm^3. Fineness modulus is a measurement of the coarseness of an aggregate. A higher value of fineness modulus represents a coarser aggregate. Fig. 1(e) shows the image of the FAC under a microscope. Using micro silica fume in the mixtures is to enhance the bond strength of the ITZ (interface transition zone) between FAC and cement paste. The rubber powder is produced by grinding scrap tyres. The density of rubber powder with average particle size of 425μm, 250 μm and 150μm are 342 kg/m^3, 326 kg/m^3 and 318 kg/m^3, respectively. Fig. 1(c) shows the picture of rubber powder while Fig. 1(d) shows the image of rubber powder under a microscope. From Fig. 1(f), the particle distribution of rubber powder is similar to that of FAC. To obtain high tensile strain capacity, the addition of polyethylene (PE) fibers was optimized to all groups. Table 2 shows the mechanical properties of the PE fibers. Polycarboxylate-based superplasticizer was adopted to obtain the workability of the mixture and to achieve uniform fibers distribution.

In this study, 4 mixtures (including a control group) were prepared to investigate the effect of rubber size on various characteristics of ULHDCC. For all the mixtures, the PE fiber volume fraction was fixed at 0.7% while the water-to-binder ratio was 0.33. A volume fraction replacement of FAC with 5% rubber powder were selected and three particle sizes are used in the experiment. Table 3 shows the mix proportions of the ULHDCC.

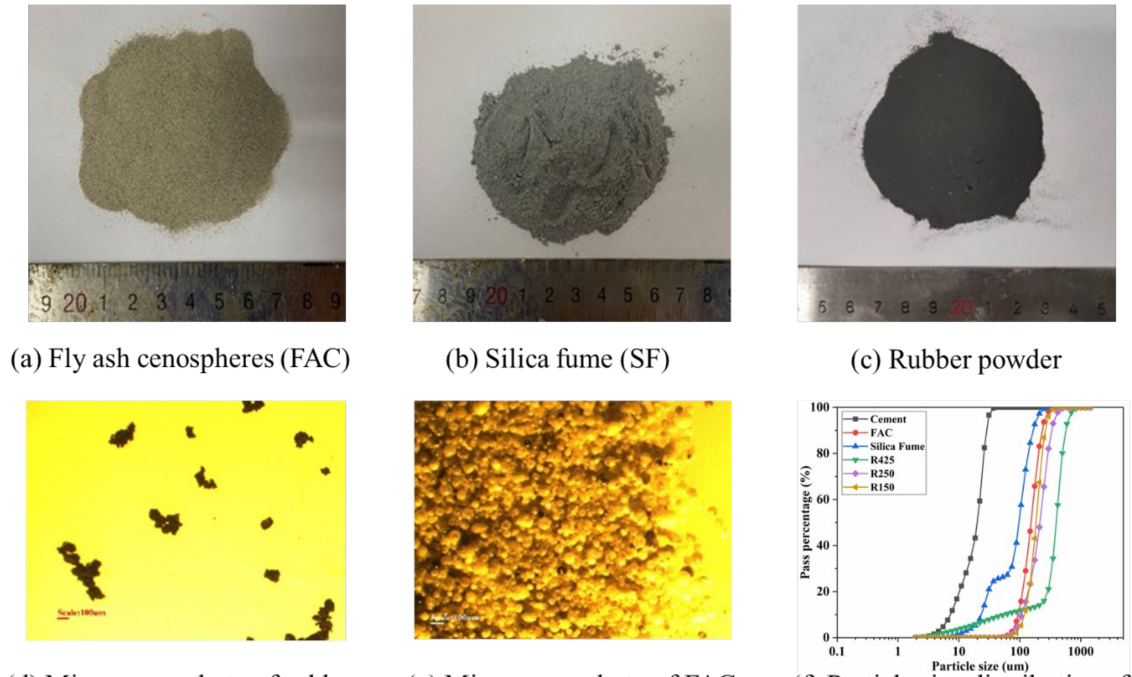

(a) Fly ash cenospheres (FAC) (b) Silica fume (SF) (c) Rubber powder

(d) Microscope photo of rubber powder (e) Microscope photo of FAC (f) Particle size distribution of raw materials

Fig. 1. Raw materials and particle size distribution.

Table 2. Mechanical properties of PE fiber.

Density (g/cm^3)	**Length (mm)**	**Diameter (μm)**	**Elastic modulus (GPa)**	**Tensile strength (MPa)**	**Fracture elongation (%)**
0.97	12	24	120	3000	2–3

Table 3. Mix design of ULHDCC.

Mix ID	**OPC**	**FAC**	**SF**	**Water**	**Rubber**	**Fiber (PE)**	**SP**	**SRA**
ULCC-0.7	702.0	339.9	78.0	259.0	0	6.8	7.0	9.0
R425-5-0.7	702.0	322.9	78.0	259.0	18.8	6.8	7.1	9.0
R250-5-0.7	702.0	322.9	78.0	259.0	18.8	6.8	7.1	9.0
R150-5-0.7	702.0	322.9	78.0	259.0	18.8	6.8	7.1	9.0

OPC = cement; SF = silica fume; SP = superplasticizer; SRA = shrinkage reducing agent.

2.2. Mixing Procedures

All the ULHDCC mixtures were prepared in a 10-liter capacity Hobart mixer. First, the raw materials were weighted, respectively, according to the mixing ratio. Cenospheres, cement, rubber powder and silica fume were then added to the mixer in sequence and low speed dry mixed for 5 minutes to ensure the powder uniformly distributed. Next, water and SP were added slowly, stirring at a low speed for 5 minutes before stirring at a high speed for 3 minutes after adding SRA. This is followed by adding the fibers and stirring the mixer to achieve an even dispersion. Finally, the fresh mixtures were placed into moulds and covered with plastic sheets at the end of initial setting. After 24 hours, the specimens were demoulded and then cured in a fog room for standard 28 days curing (temperature of 23 ± 3 °C at 95% humidity) for 28 days before testing.

2.3. Test Methods and Setup

2.3.1 Workability and density

The fluidity of each mixture was measured based on the GBT 2419-2005 [53]. The density is calculated by the water displacement method according to EN 12390-7 [54] as shown in Eq.(1)

$$\rho=\frac{m\rho_w}{m_a-m_w} \tag{1}$$

where, m is the mass of oven-dried specimen, in kg; ρ_w is the water density, taken as 1000kg/m^3; m_a is the specimen mass in air, in kg; m_w is the apparent mass of the immersed specimen, in kg.

2.3.2 Compressive test

The densities were measured on a 28-day cured cube specimen using the water displacement method. The measurement of elastic modulus and compressive strength of the ULHDCC were performed on Φ100 × 200 cylinders by 300 tones MTS machine with the loading rate of 1 mm/min, according to ASTM C39 [55] and ASTM C109 [56], respectively. Before the test, both ends of the cylindrical sample were smeared with plaster for leveling. At least three samples of each mixture were prepared for testing. Fig. 2. shows the typical setup of the elastic modulus and compression tests.

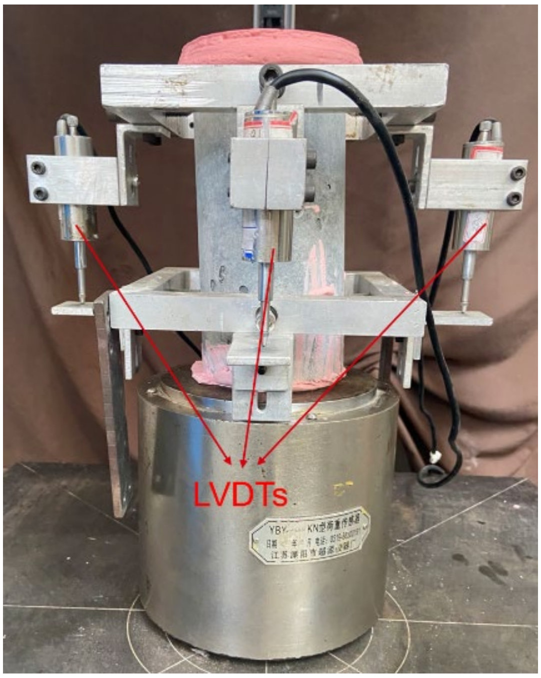

Fig. 2. Setup for the elastic modulus and compressive test.

2.3.3 Uniaxial tensile test

The dog-bone shaped specimens were used to conducted to perform the uniaxial tensile test according to JSCE standards [57]. Fig. 3 shows the test setup for uniaxial tensile and dimensions of the dog-bone specimen. At least four dog-bone shaped specimens were prepared for each mix proportion to obtain 28-day tensile properties of the ULHDCC. The tensile test was conducted with a loading rate of 0.2mm/min. Linear variable differential transducers (LVDTs) were used to record the full range of stress-strain curves of the ULHDCC. The gauge length is 80 mm.

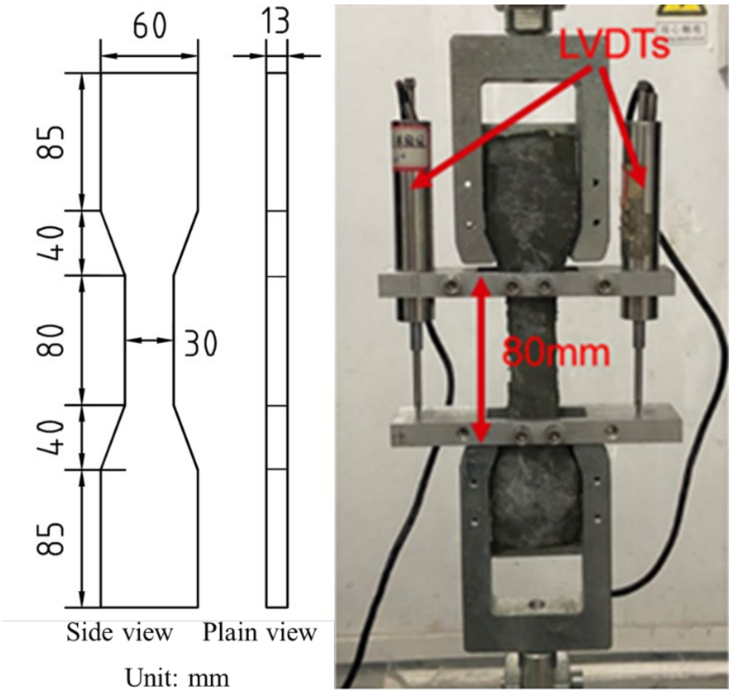

Fig. 3. Test setup for tensile test and dimensions of dog-bone specimen.

2.3.4 Three-point bending test

Typical three-point bending tests were conducted on notched beams of 40mm(W)×40mm(H)×160mm(L) to evaluate the fracture toughness of the matrix. The test setup and specimen size are shown in Fig. 4. The beams were prepared according to the mixture design as shown in Table 3 without fiber added. A pre-notch of 16mm in depth was cut at the mid-span. The notch depth/beam height ratio was set to 0.4. The loading rate was set to 0.1mm/min.

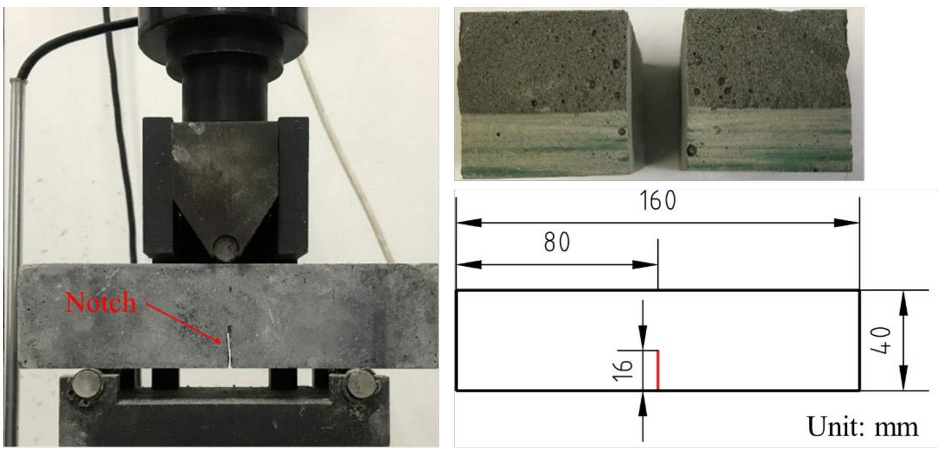

Fig. 4. Three-point bending test setup and dimension of notched beam.

2.3.5 Single-crack tensile test

A single-crack tensile test was carried out to obtain the relationship ($\sigma - \delta$ curve) between the bridging stress (σ) and the crack opening (δ) of the ULHDCC. Before the test, a cut of smaller than 1mm in width was prepared in the middle of the dog-bone shaped specimen by a saw to generate a single crack and prevent the creation of additional cracks inside or outside the cut, as shown in Fig. 5. Ideally, when a tensile load is applied, a crack should appear at the notch. Fig. 5 shows the dimensions of the specimen and the test setup for single-crack tension. In the test, an extensometer with a gauge length of 5 mm was attached to collect the change of the crack opening.

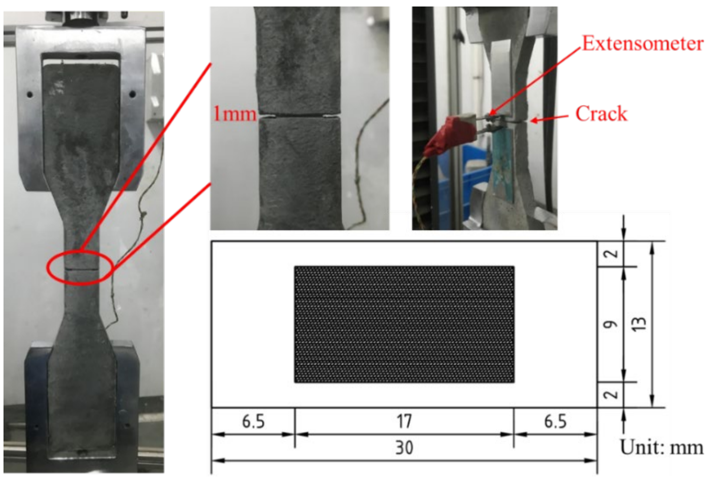

Fig. 5. Single-crack tensile test setup and specimen dimension.

2.3.6 SEM and MIP test

The morphology of the specimen was studied using the Environmental Scanning Electron Microscope (ESEM) images taken by a Quanta™ TM250 SEM. ESEM can examine different content of water phase without damage [58]. The ESEM operated at 10 kV, at a pressure of 10 Pa using a spot size of 3.0. The ESEM specimens were prepared by removing small pieces on the fractured surface from the dog-bone specimen after uniaxial tension test.

The Poremaster-60 Mercury Intrusion Porosimetry (MIP) was utilized to evaluate the total porosity and pore structure of the cement composites. The composite samples were cured for

28 days before they were broken into small pieces and immersed in absolute ethanol to terminate further hydration. The samples were then dried in a vacuum oven for 48 hours at a temperature of 60°C.

3. Experimental Results and Discussions

3.1. Density and workability

Figure. 6 shows the flow table test for the composites. For ULCC-0.7, R425-5-0.7, R250-5-0.7 and R150-5-0.7, the average flow diameters of each group are 185mm, 195mm, 200mm and 197mm, respectively. Although rubber particles negatively affect the fluidity of the fresh ULHDCC [47], after adding the appropriate amount of superplasticizer, all ULHDCC have excellent workability with a slump flow of about 185-200mm. The density of the ULHDCC is between 1295 kg/m^3 and 1332kg/m^3, which is less than 1950 kg/m^3 as required by the Chinese standard JGJ 51-2002 for lightweight concrete [1]. Among them, the density of the mixture with rubber powder is significantly lower than that without rubber powder. One of the reasons is that the more pores, due to the agglomeration effect and the hydrophobicity of rubber powders, are produced in the cement matrix in the process of mixing.

Fig. 6. Slump flow test for ULHDCC.

3.2. Compressive strength and elastic modulus

Fig. 7 shows the compressive strength and elastic modulus of ULHDCC. Compared with ULCC-0.7, the compressive strengths of R425-5-0.7, R250-5-0.7 and R150-5-0.7 are reduced by 13.1%, 19.1% and 16.3%, respectively while the elastic modulus decreased by

16.8%, 15.1% and 14.3%, respectively. After adding rubber powder in the composites both reduced the compressive strength and elastic modulus. However, it appears that particle size of the rubber powder has no obvious effect on the strength and elastic modulus at 5% rubber powder admixture. This may depend on the larger dosage of rubber powder addition. A rubber particle has a hydrophobic surface [39] that results in a weak point between the rubber particle and the surrounding cement-based inorganic materials. This will inevitably lead to lower bonding strength of ITZ and finally weaken the compressive strength of the mixture [47]. In addition, the elastic modulus of rubber is obviously lower than that of concrete. Rubber powder deforms slowly under quasi-static load and disperses in cement-based materials as weak points. When the cenospheres in ULCC are replaced by rubber powder with lower elastic modulus, the modulus of the ULCC also decreases gradually. Fig. 8 shows the failure modes of ULHDCC after the compression test. Due to the lower elastic modulus and larger deformation of rubber, in the compression test, the specimens with rubber powder only had a few cracks on the surface without obvious falling debris, while the specimens without rubber powder were severely crushed and spalled with loud crushing noise. The addition of fiber can prevent the concrete from breaking and spalling. When the specimen is compressed, the concrete matrix is stretched in the transverse direction. The bridging effect of fibers holds the matrix in the cement-based material together, thereby effectively improving the integrity of the specimen.

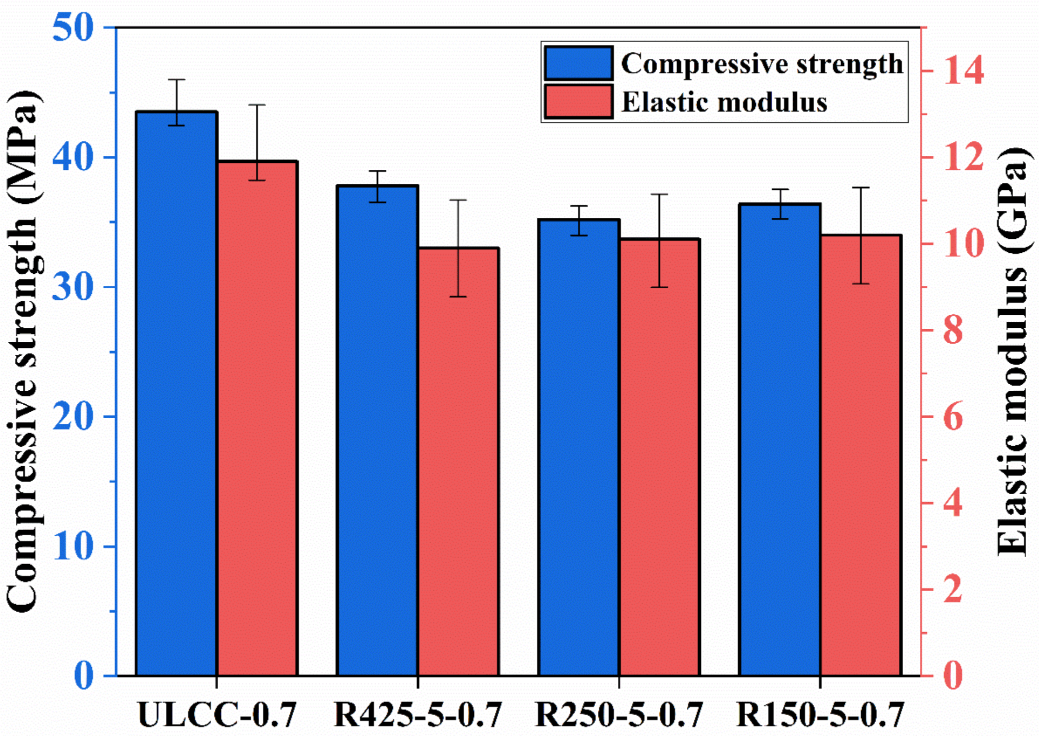

Fig. 7. Compressive strength and elastic modulus of ULHDCC.

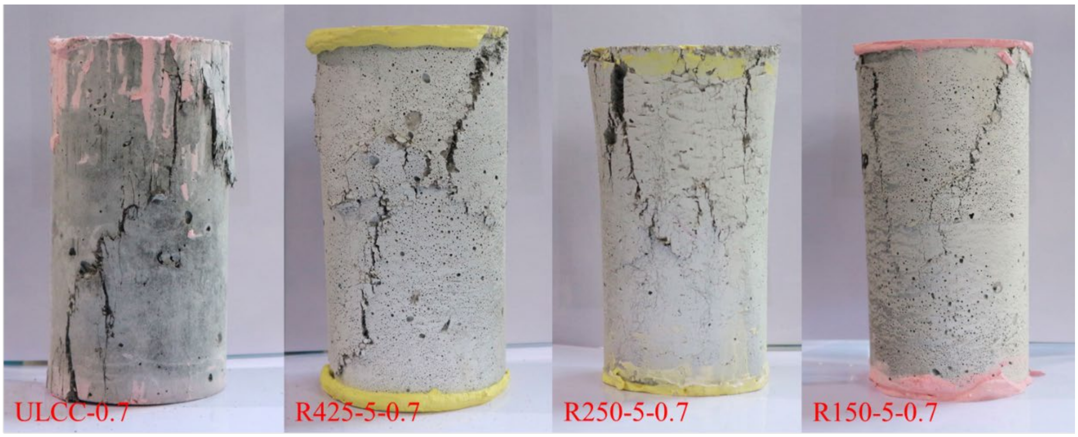

Fig. 8. Failure modes of ULHDCC samples.

3.3. Tensile ductility

Figure 9 shows the typical tensile stress-strain curves of the ULHDCC. It can be seen from the figure that all mix design exhibits excellent strain-hardening behavior. The tensile strength of each group is about 3.5 MPa, and the strain is more than 3%. Since the strain capacity is related to the number of cracks and the average crack width, the crack mode is critical for ECC. The crack mode of the ULHDCC is shown in Figure 10, while Table 4 lists the number of cracks and average crack widths. The crack number was only measured within the gauge length (80mm) of the specimen. The average crack width was determined by averaging the measured crack width. The results show that each group of the mixture shows a multi-crack failure mode. R425-5-0.7 has the largest crack number of 23 and has the smallest average crack width of 185um, which are smaller than the cracks in other mixtures. The spacing between adjacent cracks is smaller and closer to the saturated crack state, which improve the strain capacity. The stress-strain curves show that the ULHDCC exhibits superior tensile properties. Figure 11 shows the effect of fiber content on the tensile strain capacity of ULHDCC and conventional ECCs. The strain capacity of the R425-5-0.7 group is higher than 5% with only 0.7% fibers. Compared with conventional ECCs, ULHDCC developed in this study has reduced the fiber content by 65% but remaining a tensile strain of higher than 3%. The tensile strain even exceeds that of ECCs with 2% fibers. Therefore, the ULHDCC is a novel cost-effective material with superior mechanical properties.

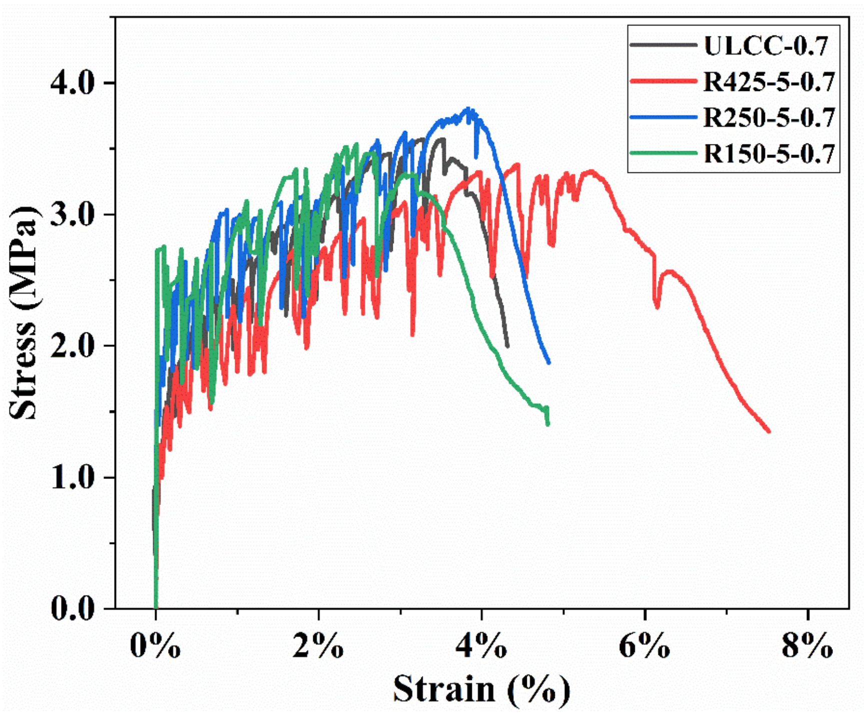

Fig. 9. Tensile stress-strain curve of ULHDCC.

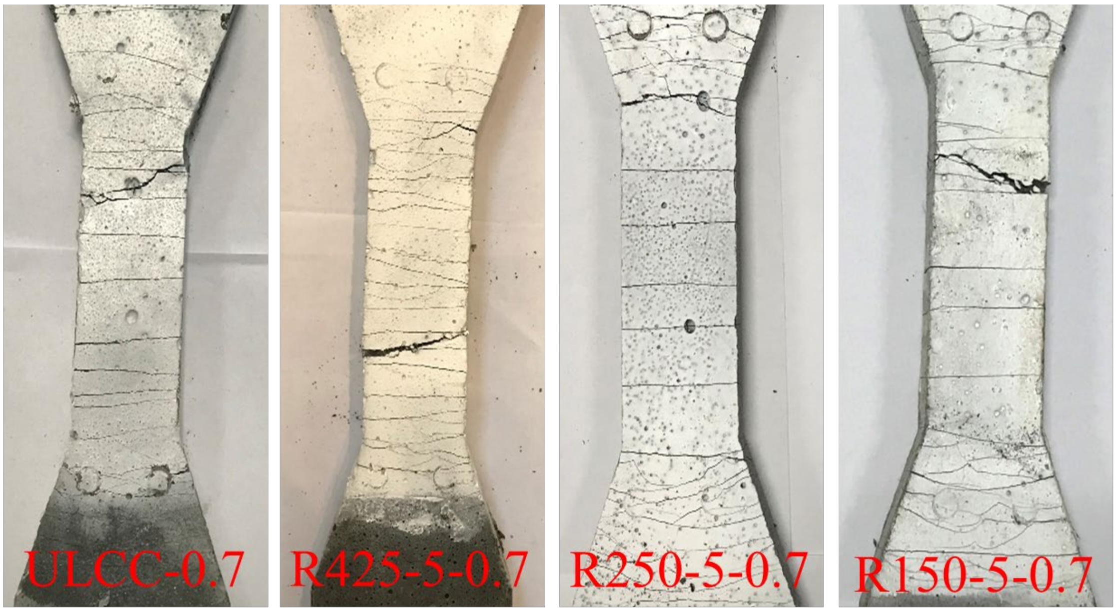

Fig. 10. Failure morphology after tensile test.

Table 4. Crack pattern of ULHDCC mixtures.

Item	ULCC-0.7	R425-5-0.7	R250-5-0.7	R150-5-0.7
Number of cracks	12±2	23±3	11±2	10±2
Average crack width (um)	234	185	278	253

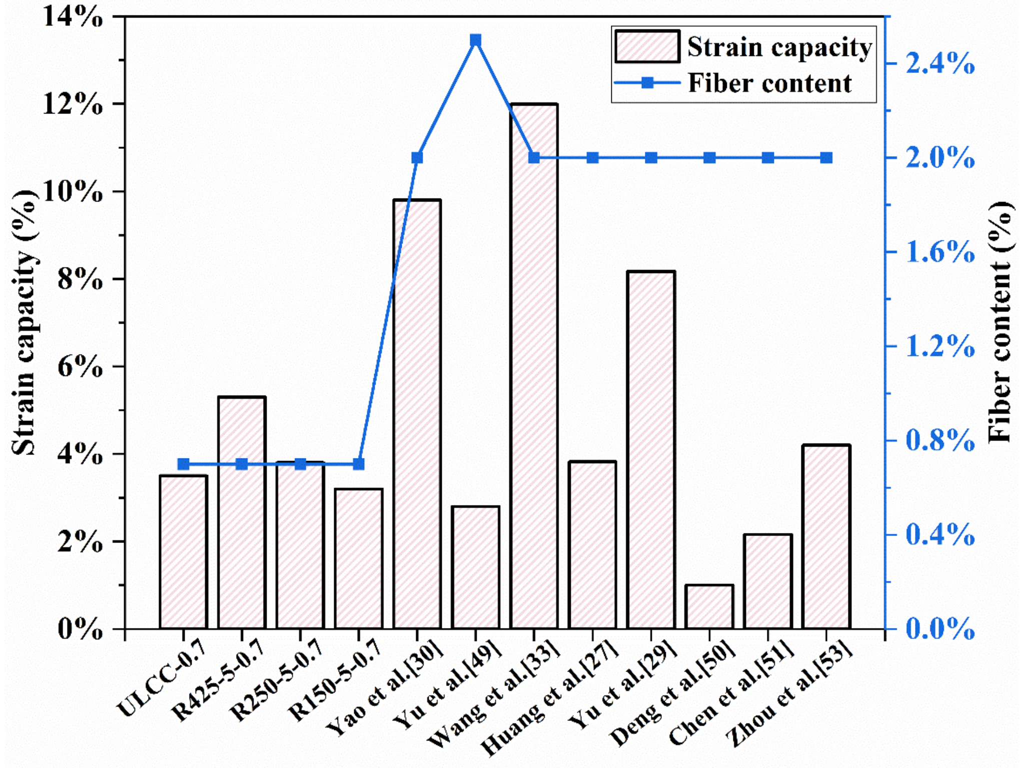

Fig. 11. Fiber content vs. strain capacity of different ECCs.

Figure 12 shows a typical tensile stress-strain relation for ULHDCC [30]. Five key

σ_{tc}), first-cracking strain (ε_{tc}), peak stress (σ_{tu}),

ε_{tu}), and strain energy (g_{se}), can be used to represent the strain hardening behavior of ULHDCC. The first-cracking stress σ_{tc} represents the turning point from the linear elastic part to the strain hardening part of the curve. The value of first-cracking stress σ_{tc} is determined from the starting point of the strain hardening branch of the curve. The strain energy g_{se} is defined as the area enclosed the stress-strain curve up to the peak stress and the two coordinate axes. The details of the above five parameters are summarized in Table 5.

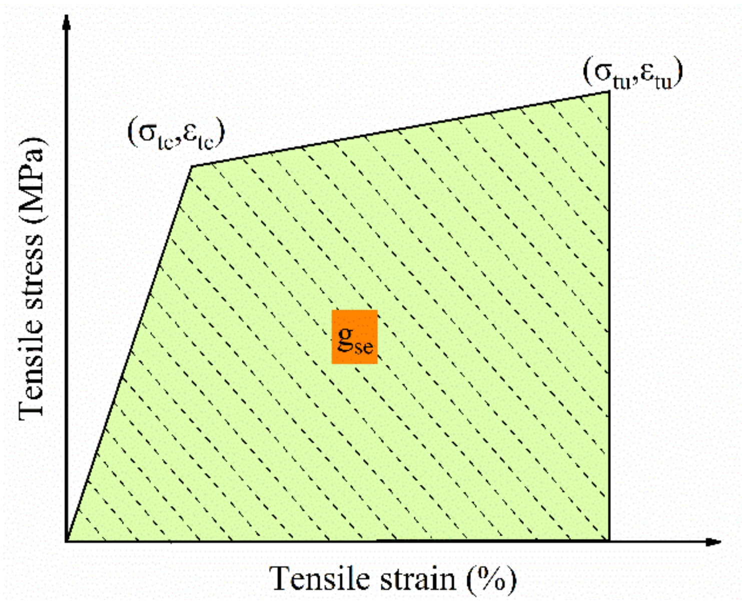

Fig. 12. Typical stress-strain relationship of high ductility composite [30].

Table 5. Summary of the average tensile parameters of ULHDCC

MIX ID	First-cracking stress $\sigma_{tc}\,(MPa)$	First-cracking strain $\varepsilon_{tc}\,(\%)$	Peak stress $\sigma_{tu}\,(MPa)$	Strain capacity $\varepsilon_{tu}\,(\%)$	Energy dissipation capacity $g_{se}\left(kJ\cdot m^{-3}\right)$
ULCC-0.7	0.95	0.019	3.57	3.506	97
R425-5-0.7	1.25	0.040	3.38	5.330	139
R250-5-0.7	1.65	0.028	3.81	3.829	116
R150-5-0.7	2.72	0.019	3.53	3.161	92

Note: These data were obtained from the average value of three samples.

As shown in Table 5, a decrease of rubber particle size leads to a decrease of first-cracking strain, strain capacity and strain energy, while an increase of first-cracking stress. The initial cracking stress increases from 0.95MPa (ULCC-0.7) to 2.72MPa (R150-5-0.7). The first-cracking strength is partly related to the size of voids of the matrix. It is because the particle size of rubber powder (150um and 250um) is with the same scale of cenospheres, which can fill the voids and improve the microstructure of the matrix. However, a higher first-cracking strength indicates that a relatively higher external energy is needed to generate new cracks, which leads to a lower pseudo strain-hardening index (PSH) [59]. The detailed description of PSH will be discussed in Section 3.4. The tensile strength of the ULHDCC is around 3.38 to 3.81MPa as shown in Table 5. The tensile strength is determined by the fiber bridging capacity, which is further affected by the fiber properties and fiber/matrix interface. The decrease in tensile strength of R425-5-0.7 mixture may be due to the incorporation of larger size of rubber powder. The addition of rubber has created more air voids and increased the porosity of the matrix, resulting in the decrease of bond between fibers and matrix [39]. The results also show that the strain energy increases with the addition of rubber powder, and R425-5-0.7 has the highest strain energy among these mixtures.

3.4. Strain hardening interpretation of ULHDCC with low fiber content

In this study, cenospheres were used as fine aggregate in the ULHDCC to achieve high strength and low density. The strain hardending behavior of the ULHDCC was improved by adding 0.7% PE fibers and replacing 5% rubber powder of different particle size. To verify and explain the strain hardening behavior of the ULHDCC with low fiber content, the micromechanics-based theoretical model [60, 61] is introduced. The model requires that ECC should meet two criteria, namely strength and energy criteria, to achieve the strain hardening behavior. The strength criterion requires that the initiating crack strength σ_{fc} must be less than the maximum bridging stress σ_0. The energy criterion requires that the energy needed for the crack propagation in matrix J_{tip} must be lower than $J_b^{'}$ (complementary energy) to promote crack development and generate multiple cracks. Figure 13 shows the bridging stress σ versus crack opening δ, J_{tip} and $J_b^{'}$ are calculated based on Eqs. (2) - (3)[61].

$$J_{tip} \le J_b^{'} \equiv \sigma_0\delta_0 - \int_0^{\delta_0} \sigma(\delta)\, d\delta \tag{2}$$

$$J_{tip} \cong K_m^2 / E_m \tag{3}$$

where σ_0 and δ_0 are the fiber bridging stress and the corresponding crack opening. E_m is the elastic modulus of the matrix. K_m is the fracture toughness, while K_m is obtained by three-point bending tests on notched beams, following Eq. (4)[62].

$$K_m = \frac{1.5\left(F_Q + \frac{mg}{2} \times 10^{-2}\right) \times 10^{-3} \times S \times a_0^{1/2}}{th^2} f(a) \tag{4}$$

where

$$f(a) = \frac{1.99 - a(1-a)\left(2.15 - 3.99a + 2.7a^2\right)}{(1+2a)(1-a)^{3/2}} \tag{5}$$

and

$$a = \frac{a_0}{h} \tag{6}$$

where F_Q is the peak load in the three-point bending test; m is the specimen mass; g is the gravitational acceleration; t is the beam width; h is the thickness of the beam, S is the clear span of the beam; a_0 is the depth of the internal notch; and $f(a)$ is the shape parameter of the beam.

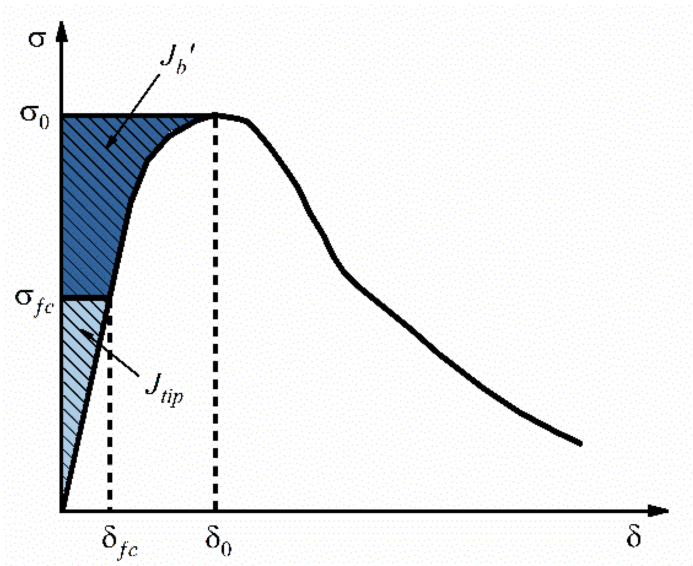

Fig. 13. Typical bridging stress-crack opening curve for composite.

To achieve saturated PSH, Kanda and Li [63] proposed two perforamnce index, namely, stress and energy performance index as presented in Eqs. (7-8) to represent the strain hardening behavior.

$$PSH_{(strength)} = \sigma_0 / \sigma_{fc} \quad (7)$$

$$PSH_{(energy)} = J_b^{'} / J_{tip} \quad (8)$$

Based on extensive experimental verification and theoretical analysis, the following recommendations were proposed for materials of high strain-hardening performance

$$PSH_{(strength)} > 1.2 \text{ and } PSH_{(energy)} > 3 \, [63] \quad (9)$$

$$PSH_{(strength)} > 1.3 \text{ and } PSH_{(energy)} > 2.7 \, [64] \quad (10)$$

$$PSH_{(strength)} > 1.5 \text{ and } PSH_{(energy)} > 3 \, [65] \quad (11)$$

In this study, the target value of *PSH* indeies were set as $PSH_{(strength)} = \sigma_0 / \sigma_{fc} > 1.3$ and $PSH_{(energy)} = J_b^{'} / J_{tip} > 3$ to determine the high strain-hardening properties of the ULHDCC.

From the single-crack tensile test on the notched beam, the stress-crack opening curves is shown in Fig. 14. The peak stress reduced by the addition of rubber powder, while the effect of rubber particle size on the peak stress is marginal. Table 6 presents the relationship

σ_0 and the crack-opening δ_0. The values of PSH(strength) are calculated by Eq. (7) and presented in Table 6. The PSH(strength) of all the mixtures are larger than 1.3. It can be seen from Table 6 that after adding rubber powder, the first crack stress, σ_{fc}, increases and the maximum fiber bridging capacity, σ_0, decreases, leading to the decrease of the PSH(strength) (Eq. (7)). A larger PSH(strength) is an indication of saturated multiple cracking. Compared with different size of rubber powder, the mix design with particle size of 425um has highest PSH(strength). The mixtures using finer particle size all have lower PSH(strength), which indicates that use of very fine rubber powder is not always beneficial. Use of less fine powder also save grinding energy.

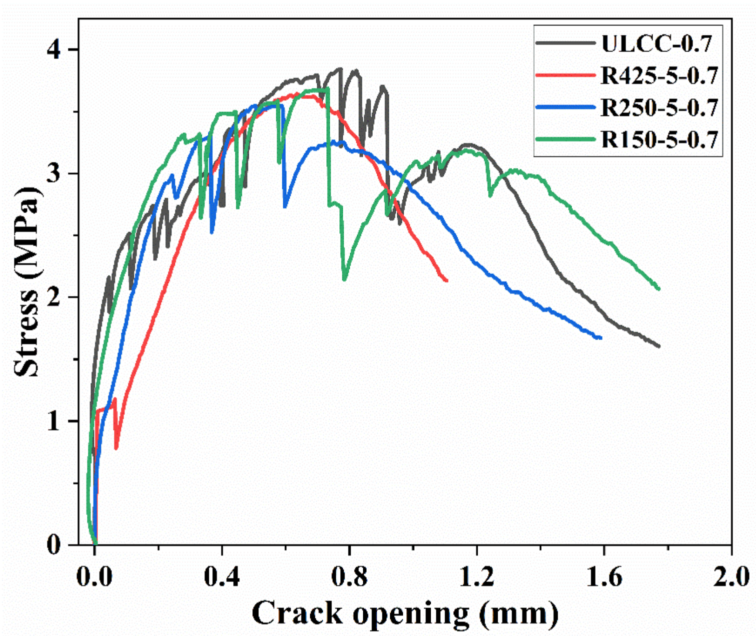

Fig. 14. Uniaxial tensile stress–crack opening curves of ULHDCC.

Table 6. Test results of single-crack tensile test.

MIX ID	$\sigma_0\,(MPa)$	$\delta_0\,(mm)$	$\sigma_{fc}\,(MPa)$	$PSH_{(strength)}$
ULCC-0.7	3.83	0.82	0.95	4.03
R425-5-0.7	3.62	0.64	1.25	2.90
R250-5-0.7	3.57	0.59	1.65	2.16
R150-5-0.7	3.65	0.72	2.72	1.35

Table 7 presents the fracture toughness of cement composites based on three-point bending

K_m, the complementary energy $J_b^{'}$ and

the crack tip energy J_{tip}

that the crack tip energy J_{tip} and the fracture toughness K_m both decrease with the addition of rubber powder.

Table 7. Fracture toughness of cement composites.

MIX ID	$m(g)$	$F_Q(N)$	$K_m\left(MPa \cdot mm^{1/2}\right)$	$J_{tip}\left(J/m^2\right)$	$J_b^{'}\left(J/m^2\right)$	$J_b^{'}/J_{tip}$
ULCC-0.7	361.0	904.3	17.745	22.49	589.93	26.23
R425-5-0.7	351.0	589.6	11.581	7.69	722.26	93.92
R250-5-0.7	344.5	591.1	10.843	5.25	481.70	91.75
R150-5-0.7	335.0	576.4	12.144	9.84	441.17	44.83

The pseudo-strain hardening indices, $PSH_{(energy)}$, of the ULHDCC were calculated according to Eq. (8). Fig.15 compares the $PSH_{(energy)}$ between the ULHDCC and the normal ECCs. The $PSH_{(energy)}$ values of all the mixtures are higher than the recommended value of 3.0 for the design of strain-hardening cement composites. The $PSH_{(energy)}$ of the ULHDCC increases significantly when rubber powder are added. With the increase of rubber particle size, $PSH_{(energy)}$ also increases, which is beneficial to the plasticity of the composite. The $PSH_{(energy)}$ of R425-5-0.7 group achieves the largest value of 93.9, which verifies that the R425-5-0.7 group exhibits the best strain hardening.

To ensure that ECC have more saturated microcracks and higher tensile strain capacity, it

J_{tip} and the

complementary energy $J_b^{'}$ [66]. A larger strain hardening index $PSH_{(energy)} = J_b^{'}/J_{tip}$

fracture toughness K_m of the matrix decreases by 32% - 39%, the crack tip energy J_{tip} decreases by 56% - 77%, and the complementary energy $J_b^{'}$ decreases by 18%-25% (except R450-5-0.7). However, the resulting $J_b^{'}/J_{tip}$ ratio increases significantly. Therefore, the ULHDCC is more likely to produce new cracks under tension, which ensures the occurrence of multiple cracks. Among them, only when adding 425um rubber powder, the value of $J_b^{'}$ increases by 22%. Therefore, for mixture R425-5-0.7, J_{tip} decreases while $J_b^{'}$ increases. The combined effect leads to the increase of $J_b^{'}/J_{tip}$ ratio, which helps the occurrence of saturated multiple cracking and higher strain capacity. Compared with other ECCs, the $PSH_{(energy)}$ value of the ULHDCC with PE fiber content of 0.7% by volume can achieve 93.9, leading to a sufficient margin between the crack tip energy J_{tip} and the complementary energy $J_b^{'}$. The low fiber content of the ULHDCC also offers a more cost effective material than normal ECCs.

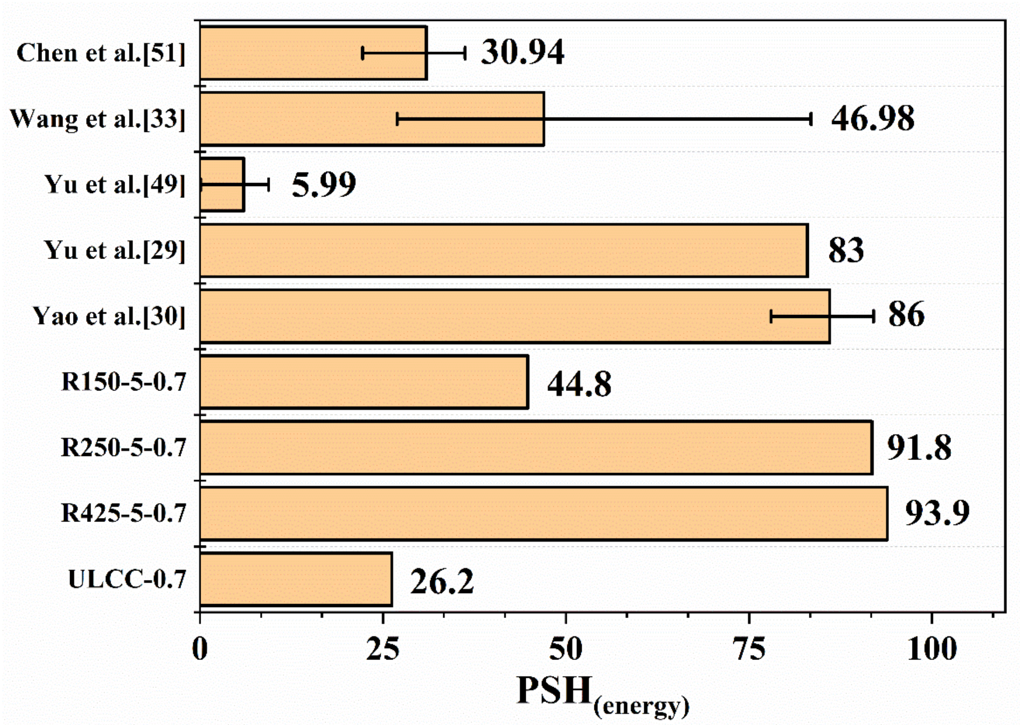

Fig.15. $PSH_{(energy)}$ values of different mixtures.

3.5. Pore structure

Two mixtures, ULCC-0.7 and R425-5-0.7, are selected to study the pore structure of the ULHDCC. The porosities of ULCC-0.7 and R425-5-0.7 are 52.57% and 55.06%, respectively. The addition of rubber powder increases the porosity, which also reflects that the addition of rubber reduces the compressive strength of the mixture. Figure 16 illustrates the pore size distribution and pore volume distribution of the mixtures. The pore size distribution curves reflect the pore volume of different pore sizes, as shown in Figure 16(a). The characteristic peaks of the two mixtures are mainly in the range of 0.01um-0.02um. The critical pore diameter can be determined by the diameter corresponding to the peak value of pore size distribution curve [67]. It is the most common diameter of interconnected pores, which maximizes penetration of chemical substances through cement matrix [68]. After adding rubber powder, the critical pore diameter increased from 0.01303 um to 0.0141um. Therefore, the addition of rubber powder produces more interconnected pores in the cement matrix, which also leads to the increase of porosity. Based on the pore size, the pores in the composite are divided into gel pores (< 0.01um), medium capillary pores (0.01um-0.5um), large capillary pores (0.5um -10um) and macro-pores (>10 um) [69]. Figure 16(b) shows the pore volume fraction of the two mixtures. The pore diameters are divided into four categories as described above. Both samples have the largest proportion of medium capillary pores, accounting for about 50%. After adding rubber powder, the proportions of gel and medium capillary pores decrease by 6.78% and 5.16%, respectively. The proportion of large capillary pores increases by 2.17%, and the proportion of macro-pores increases by 9.78%. The proportion of small pores in the mixture decreases, while the proportion of large pores increases. The average pore size increases from 0.01699um to 0.02410um, leading to a higher porosity.

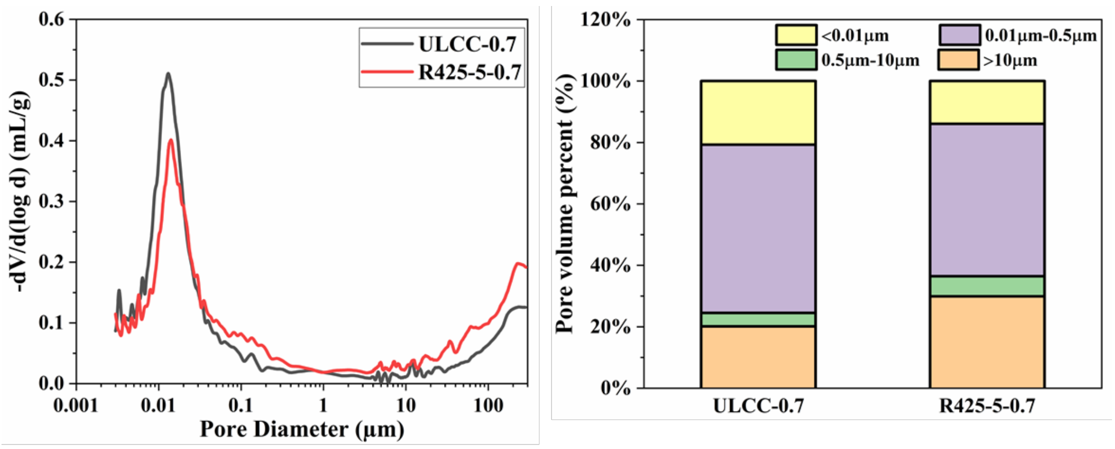

(a) (b)

Fig. 16. Pore structure of ULHDCC (a) pore size distribution curves, (b) pore volume distribution.

3.6 ESEM of ULHDCC

Figure 17 shows the ESEM images of the ULHDCC at 28 days. Fig.17(a) shows that the cenospheres and rubber powder are loosely distributed in the cement matrix, and ITZ is formed between the aggregate and the matrix. The reason is that the cenospheres are filled with inert gas and the surfaces of the rubber powders were hydrophobic. A large number of air bubbles are introduced during the stirring process, forming a porous microstructure at the aggregate/matrix and fiber/matrix interface, leading to an increase of porosity in the composites and reductions in the matrix toughness and fiber bridging strength. In addition, the spherical shape of the cenospheres plays a "ball effect" in improving the rheological properties of the fresh cement paste and the fiber dispersion [71].

In Figure 17(b), numerous PE fibers are pulled out from the cement matrix. The friction between the fibers and matrix causes damage and fibrillation of the fibers. There are obvious scratches or even wiredrawing on the surface of the PE fibers, as shown in Fig.17(c) and 17(d), which reduces the effective cross-sectional area of the fibers. Figure 17(e) shows a large amount of hydration products and that FAC fragments are attached to the surface of the PE fibers. It can effectively increase the friction between the PE fiber and the matrix during the stretching process, leading to increased bonding strength between the fiber and matrix. After the PE fibers are pulled out or broken, they are obvious grooves in the cement matrix, as shown in Fig. 17(f). Microcracks may develop along the interface between the matrix and the cenospheres or rubber particles. There may be also some damaged cenospheres or rubber powders. The ESEM image shows the configuration of the interface between rubber powder/cenospheres and cement composites, as well as the typical failure mode of PE fiber.

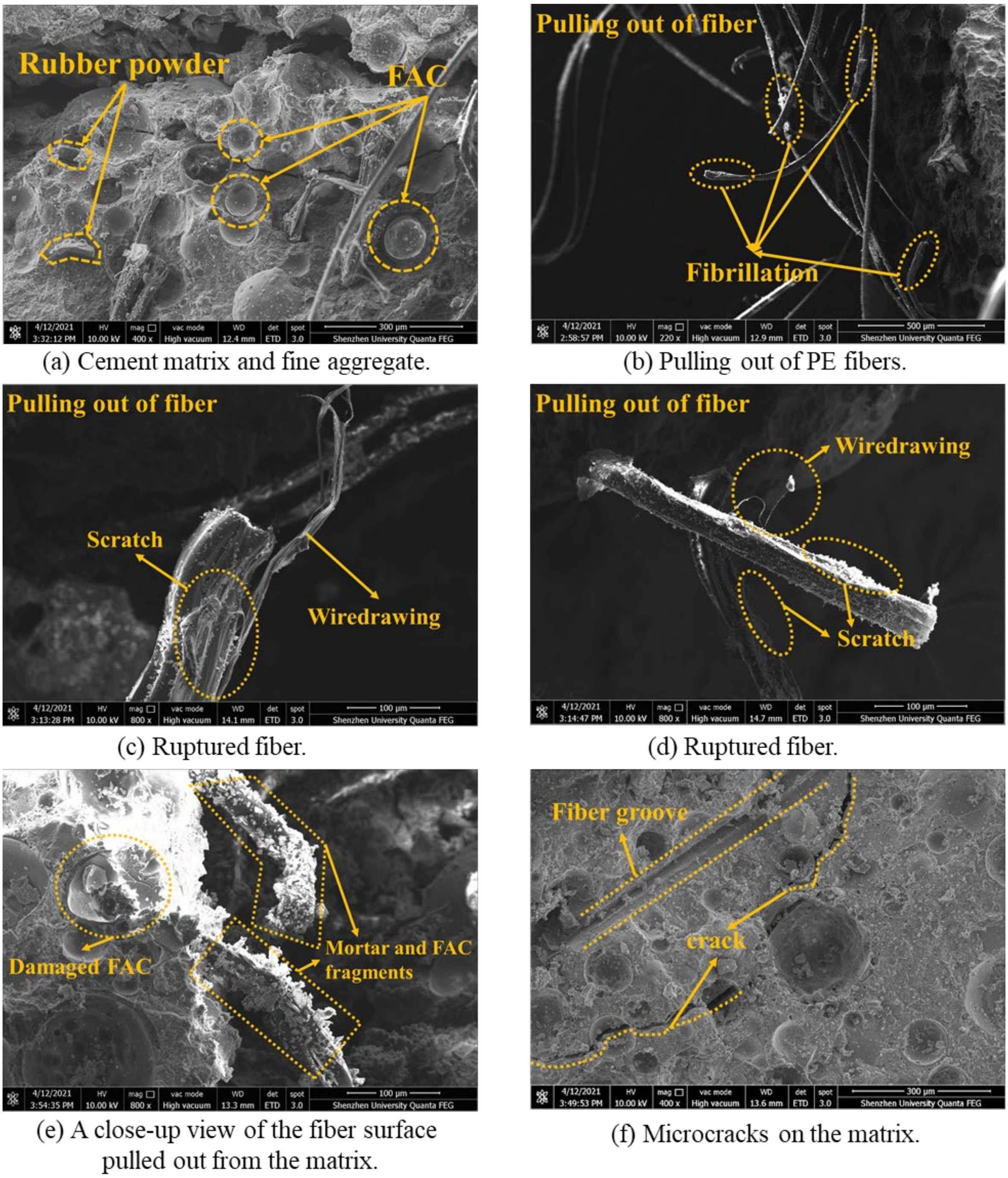

(a) Cement matrix and fine aggregate. (b) Pulling out of PE fibers.
(c) Ruptured fiber. (d) Ruptured fiber.
(e) A close-up view of the fiber surface pulled out from the matrix. (f) Microcracks on the matrix.

Fig.17 ESEM image of ULHDCC.

4. Economy assessment of ULHDCC

The contents of fibers, rubber powder and cenospheres in the ULHDCC determine the mechanical properties and also the cost of the composites. Figure 18(a) shows the unit price of the raw materials (based on Shenzhen market, China) [72]. The total cost of the four mixtures is compared with that of the conventional ECCs, as shown in Fig. 18(b). Compared with the ordinary concrete, the increased cost of ECCs mainly comes from fiber and high cement content. Therefore, the volume of fiber and cement needs to be reduced to reduce the overall cost of ECCs. ULHDCC mainly reduces the cost by reducing the amount of fiber while maintaining the high ductility of ECC. The cost of fiber accounts for more than three-quarters of the total ECC cost. For comparable strain capacity and strain hardening, the required fiber content in the ULHDCC is 0.7%, which is only one half of that in conventional ECCs.

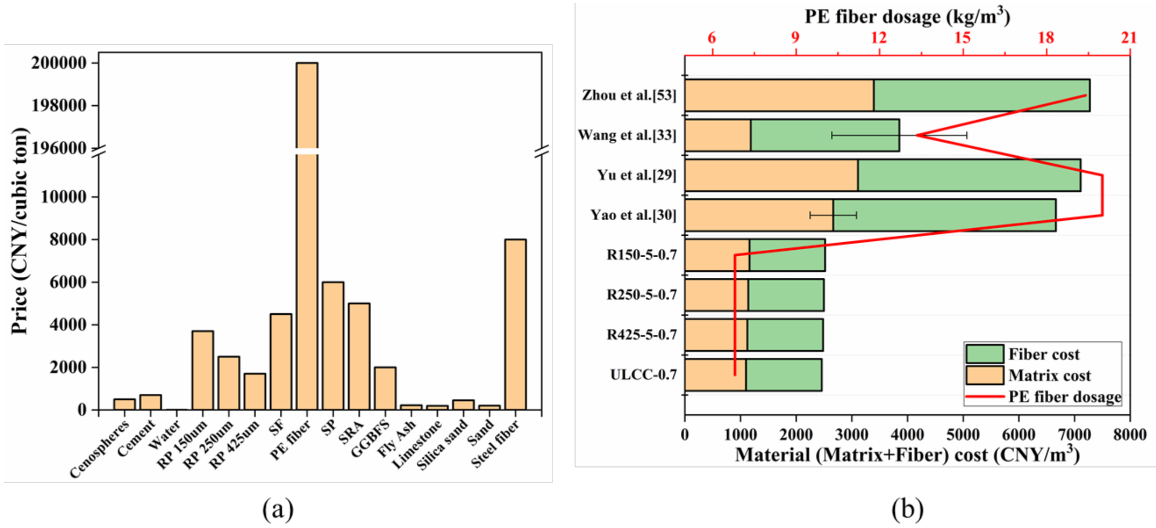

Fig. 18. Economy assessment of (a) Unit price of Constituents. (b) Comparison of material cost of different mixtures.

5. Conclusions

The present study developed a novel ultra-lightweight high ductility cement composite (ULHDCC) using cenospheres, rubber particles, and PE fibers. The microstructure and mechanical properties of the ULHDCC were comprehensively investigated. The use of rubber powder and low PE fiber content resulted in excellent strain hardening and cost reduction. The main conclusions are summarized as follows:

1. ULHDCC exhibits high $PSH_{(strength)}$ index of greater than 1.3, and high $PSH_{(energy)}$ index of greater than 3.0, which ensure superior ductility of the composites. Mixture R425-5-0.7 has

the best strain hardening among the designed mixtures, which can be used as a guideline for designers to reduce ECC fiber and material costs.

2. ULHDCC has a very low density but with high compressive strength of above 30 MPa, which can be used for structural concrete. By adding rubber powder and 0.7% PE fiber, the ULHDCC has a tensile strength of 3.5MPa with a strain capacity of more than 3%.

3. The addition of rubber powder to ULHDCC reduces the toughness of the cement matrix, the crack tip energy and the complementary energy. The combined effect leads to the increase of $J_b^{'}/J_{tip}$ ratio, which helps to produce saturated multiple cracking and improves strain hardening.

4. ESEM images show initiation and propagation of micro cracks from the ITZ to the matrix. The fiber morphology after being pulled out demonstrate that the ULHDCC has outstanding pull-out and high strain capacity. MIP test show that the addition of rubber to the ULHDCC can increase matrix porosity, critical pore diameter and average pore diameter, which contributes to the decrease of the strength at the macro level.

5.ULHDCC is more economical than conventional ECCs. Low PE fiber content of 0.7% in the ULHDCC mixture leads to a significant reduction (by about 60%) of the cost, making the material a better alternative in a wider range of applications.

Acknowledgments: The authors would like to acknowledge the research grant received from National Natural Science Foundation of China (No. 51978407), Shenzhen International Science and Technology Cooperation Project (No. GJHZ20200731095802008) and Natural Science Foundation of Guangdong Province (No. 2021A1515010932).

Data Availability Statement

All data, models, and code generated or used during the study appear in the submitted article.

Conflict of Interest

The author confirms that there is no conflict of interest.

References

[1] CS (Chinese Standard) JGJ 51-02, Technical specification for lightweight aggregate concrete, 2002 (in Chinese).

[2] Y.W. Zhou, X.M. Liu, F. Xing, H.Z. Cui, L.L. Sui, Axial compressive behavior of FRP-confined lightweight aggregate concrete: An experimental study and stress-strain relation model, Constr. Build. Mater. 119 (2016) 1-15.

[3] Z.Y. Huang, K. Padmaja, S. Li, J.Y.R. Liew, Mechanical properties and microstructure of ultra-lightweight cement composites with fly ash cenospheres after exposure to high temperatures, Constr. Build. Mater. 164 (2018) 760-774.

[4] Z.Y. Huang, F. Wang, Y.W. Zhou, L.L. Sui, P. Krishnan, J.Y.R. Liew, A novel, multifunctional, floatable, lightweight cement composite: development and properties, Mater. 11(10) (2018) 2043.

[5] Z.Y. Huang, J.Y.R. Liew, W. Li, Evaluation of compressive behavior of ultra-lightweight cement composite after elevated temperature exposure, Constr. Build. Mater. 148 (2017) 579-589.

[6] Z.Y. Huang, J.Y.R. Liew, Nonlinear finite element modelling and parametric study of curved steel–concrete–steel double skin composite panels infilled with ultra-lightweight cement composite, Constr. Build. Mater. 95 (2015) 922-938.

[7] T.A. Holm, T.W. Bremner, J.B. Newman, Concrete bridge decks: lightweight aggregate concrete subject to severe weathering, Concr. Int. 6(6) (1984) 49-54.

[8] Q.X. Jin, V.C. Li, Development of lightweight engineered cementitious composite for durability enhancement of tall concrete wind towers, Cem. Concr. Compos. 96 (2019) 87-94.

[9] Z.Y. Huang, J.Y. Wang, J.Y.R. Liew, P.W. Marshall, Lightweight steel–concrete–steel sandwich composite shell subject to punching shear, Ocean. Eng. 102 (2015) 146-161.

[10] A. Lotfy, K.M.A. Hossain, M. Lachemi, Lightweight self-consolidating concrete with expanded shale aggregates: Modelling and optimization, Int. J. Concr. Struct. Mater. 9(2) (2015) 185-206.

[11] W.J. Long, X.W. Tan, B.X. Xiao, N.X. Han, F. Xing, Effective use of ground waste expanded perlite as green supplementary cementitious material in eco-friendly alkali activated slag composites, J. Clean. Prod. 213 (2019) 406-414.

[12] D.S. Babu, K.G. Babu, T.H. Wee, Properties of lightweight expanded polystyrene aggregate concretes containing fly ash, Cem. Concr. Res. 35(6) (2005) 1218-1223.

[13] K.S. Chia, X.M. Liu, J.Y.R. Liew, M.H. Zhang, Experimental study on creep and shrinkage of high-performance ultra-lightweight cement composite of 60 MPa, Struct. Eng. Mech. 50(5) (2014) 635-652.

[14] K. Chia, M.H. Zhang, J.Y.R. Liew, High-strength ultra lightweight cement composite–material properties, in: Proceedings of 9th international symposium on high performance concrete design, verification & utilization, Rotorua, New Zealand, 2011, pp. 911.

[15] Z.Y. Huang, J.Y.R. Liew, M.X. Xiong, J.Y. Wang, Structural behaviour of double skin composite system using ultra-lightweight cement composite, Constr. Build. Mater. 86 (2015) 51-63.

[16] Z.Y. Huang, J.Y.R. Liew, Structural behaviour of steel–concrete–steel sandwich composite wall subjected to compression and end moment, Thin. Wall. Struct. 98 (2016) 592-606.

[17] Z.Y. Huang, J.Y.R. Liew, Steel-concrete-steel sandwich composite structures subjected to extreme loads, Int. J. Steel. Struct. 16(4) (2016) 1009-1028.

[18] V.B. Fenelonov, M.S. Mel'gunov, V.N. Parmon, The properties of cenospheres and the mechanism of their formation during high-temperature coal combustion at thermal power plans, KONA. Powder. Part. J. 28 (2010) 189-208.

[19] S.P. McBride, A. Shukla, A. Bose, Processing and characterization of a lightweight concrete using cenospheres, J. Mater. Sci. 37(19) (2002) 4217-4225.
[20] L.N. Ngu, H.W. Wu, D.K. Zhang, Characterization of Ash Cenospheres in Fly Ash from Australian Power Stations, Energ. Fuel. 21(6) (2007) 3437-3445.
[21] A. Hanif, M. Usman, Z. Lu, Y. Cheng, Z. Li, Flexural fatigue behavior of thin laminated cementitious composites incorporating cenosphere fillers, Mater. Design. 140 (2018) 267-277.
[22] V.C. Li, C.K.Y. Leung, Steady-state and multiple cracking of short random fiber composites, J. Eng. Mech. 118(11) (1992) 2246-2264.
[23] V.C. Li, Engineered Cementitious Composites Tailored Composites through Micromechanical Modeling, Can. Soc. Civil. Eng. (1998) 64-97.
[24] V.C. Li, C. Wu, S.X. Wang, A. Ogawa, T. Saito, Interface tailoring for strain-hardening polyvinyl alcohol-engineered cementitious composite (PVA-ECC), ACI Mater. J. 99(5) (2002) 463-472.
[25] V.C. Li, On engineered cementitious composites (ECC) a review of the material and its applications, J. Adv. Concr. Technol. 1(3) (2003) 215-230
[26] V.C. Li, S.X. Wang, C. Wu, Tensile strain-hardening behavior of polyvinyl alcohol engineered cementitious composite (PVA-ECC), ACI Mater. J. 98(6) (2001) 483-492.
[27] X.Y. Huang, R. Ranade, Q. Zhang, W. Ni, V.C. Li, Mechanical and thermal properties of green lightweight engineered cementitious composites, Constr. Build. Mater. 48 (2013) 954-960.
[28] Z.F. Pan, C. Wu, J.Z. Liu, W. Wang, J.W. Liu, Study on mechanical properties of cost-effective polyvinyl alcohol engineered cementitious composites (PVA-ECC), Constr. Build. Mater. 78 (2015) 397-404.
[29] K.Q. Yu, J.T. Yu, J.G. Dai, Z.D. Lu, S.P. Shah, Development of ultra-high performance engineered cementitious composites using polyethylene (PE) fibers, Constr. Build. Mater. 158 (2018) 217-227.
[30] Y. Ding, J.t. Yu, K.Q. Yu, S.l. Xu, Basic mechanical properties of ultra-high ductility cementitious composites: From 40 MPa to 120 MPa, Compos. Struct. 185 (2018) 634-645.
[31] K.Q. Yu, Y. Ding, J.P. Liu, Y.L. Bai, Energy dissipation characteristics of all-grade polyethylene fiber-reinforced engineered cementitious composites (PE-ECC), Cem. Concr. Compos. 106 (2020) 103459.
[32] H.S. Jin, S.Y. Yang, H.Y. Xu, Z.Y. Xu, F.H. Li, Y. Tian, S. Zhou, Uniaxial Tensile Performance of PP-ECC: Effect of Curing Temperatures and Fly Ash Contents, KSCE. J. Civil. Eng. 24(11) (2020) 3435-3446.
[33] Y.C. Wang, F.C. Liu, J.T. Yu, F.Y. Dong, J.H. Ye, Effect of polyethylene fiber content on physical and mechanical properties of engineered cementitious composites, Constr. Build. Mater. 251 (2020) 118917.
[34] R. Roychand, R.J. Gravina, Y. Zhuge, X. Ma, O. Youssf, J.E. Mills, A comprehensive review on the mechanical properties of waste tire rubber concrete, Constr. Build. Mater. 237 (2020) 117651.
[35] F. Liu, G.X. Chen, L.J. Li, Y.C. Guo, Study of impact performance of rubber reinforced concrete, Constr. Build. Mater. 36 (2012) 604-616.
[36] W.H. Feng, F. Liu, F. Yang, L.J. Li, L. Jing, B.Y. Chen, B. Yuan, Experimental study on the effect of strain rates on the dynamic flexural properties of rubber concrete, Constr. Build. Mater. 224 (2019) 408-419.
[37] M. Adamu, B.S. Mohammed, M.S. Liew, Effect of crumb rubber and nano silica on the creep and drying shrinkage of roller compacted concrete pavement, Int. J. GEOMATE. 15(47) (2018) 58-65.

[38] F. Hernández-Olivares, G. Barluenga, Fire performance of recycled rubber-filled high-strength concrete, Cem. Concr. Res. 34(1) (2004) 109-117.
[39] Z.G. Zhang, H. Ma, S.Z. Qian, Investigation on properties of ECC incorporating crumb rubber of different sizes, J. Adv. Concr. Technol. 3(5) (2015) 241-251.
[40] A. Adesina, S. Das, Performance of engineered cementitious composites incorporating crumb rubber as aggregate, Constr. Build. Mater. 274 (2021) 122033.
[41] H. Hong, D. Ling, B.S. Mohammed, A. Al-Fakih, M.M.A. Wahab, M.S. Liew, Y.H. Amran, Deformation Properties of Rubberized ECC Incorporating Nano Graphene Using Response Surface Methodology, Mater. 13(12) (2020) 2831.
[42] B.S. Mohammed, A.B. Awang, S.S. Wong, C.P. Nhavene, Properties of nano silica modified rubbercrete, J. Clean. Prod. 119 (2016) 66-75.
[43] H. Siad, M. Lachemi, M.K. Ismail, M.A.A. Sherir, M. Sahmaran, A.A.A. Hassan, Effect of rubber aggregate and binary mineral admixtures on long-term properties of structural engineered cementitious composites, J. Mater. Civil. Eng. 31(11) (2019) 04019253.
[44] M.K. Ismail, M.A.A. Sherir, H. Siad, A.A.A. Hassan, M. Lachemi, Properties of self-consolidating engineered cementitious composite modified with rubber, J. Mater. Civil. Eng. 30(4) (2018) 04018031.
[45] A. Kashani, T.D. Ngo, P. Mendis, J.R. Black, A. Hajimohammadi, A sustainable application of recycled tyre crumbs as insulator in lightweight cellular concrete, J. Clean. Prod. 149 (2017) 925-935.
[46] H. Zhong, E.W. Poon, K. Chen, M.Z. Zhang, Engineering properties of crumb rubber alkali-activated mortar reinforced with recycled steel fibres, J. Clean. Prod. 238 (2019) 117950.
[47] Z.Y. Huang, L.L. Sui, F. Wang, S.L. Du, Y.W. Zhou, J.Q. Ye, Dynamic compressive behavior of a novel ultra-lightweight cement composite incorporated with rubber powder, Compos. Struct. 244 (2020) 112300.
[48] J. Yu, Y.X. Chen, C.K.Y. Leung, Mechanical performance of Strain-Hardening Cementitious Composites (SHCC) with hybrid polyvinyl alcohol and steel fibers, Compos. Struct. 226 (2019) 111198.
[49] M.K. Deng, T. Li, Y.X. Zhang, Compressive performance of masonry columns confined with highly ductile fiber reinforced concrete (HDC), Constr. Build. Mater. 254 (2020) 119264.
[50] W.H. Chen, Z.F. Qi, L. Zhang, Z.Y. Huang, Effects of cenosphere on the mechanical properties of cement-based composites, Constr. Build. Mater. 261 (2020) 120527.
[51] V.C. Li, Engineered cementitious composites (ECC) material, structural, and durability performance, (2008).
[52] Y.W. Zhou, B. Xi, K.Q. Yu, L.L. Sui, F. Xing, Mechanical properties of hybrid ultra-high performance engineered cementitous composites incorporating steel and polyethylene fibers, Mater. 11(8) (2018) 1448.
[53] GB/T2419. Test method for fluidity of cement mortar, 2005, pp. 3-5 (in Chinese).
[54] British Standard, Testing hardened concrete, Compressive Strength of Test Specimens, BS EN (2019) 12390-3.
[55] ASTM C 39. Standard Test method for compressive strength of cylindrical concrete specimens. West Conshohocken. PA, 2017.
[56] ASTM C109. Standard Test Method for Compressive Strength of Hydraulic Cement Mortars. West Conshohocken. PA, 2016.
[57] Japan Society of Civil Engineers, Recommendations for design and construction of high performance fiber reinforced cement composites with multiple fine cracks. 2008, pp. 1-16.
[58] P. Stroeven, The analysis of fibre distribution in fibre reinforced cementitious materials, J. Micro. 111(3) (2011) 283-295.

[59] Z.G. Zhang, F. Yang, J.C. Liu, S.P. Wang, Eco-friendly high strength, high ductility engineered cementitious composites (ECC) with substitution of fly ash by rice husk ash, Cem. Concr. Res. 137 (2020) 106200.
[60] T. Kanda, V.C. Li, New micromechanics design theory for pseudostrain hardening cementitious composite, J. Eng. Mech. ASCE 125(4) (1999) 373-381.
[61] V.C. Li, From micromechanics to structural engineering-the design of cementitous composites for civil engineering applications, Doboku Gakkai Ronbunshu. (1993).
[62] S.L. Xu, H.W. Reinhardt, Determination of double-K criterion for crack propagation in quasi-brittle fracture, Part II: Analytical evaluating and practical measuring methods for three-point bending notched beams, Int. J. Fracture. 98(2) (1999) 151-177.
[63] T. Kanda, V.C. Li, Multiple cracking sequence and saturation in fiber reinforced cementitious composites, JCI Concr. Res. Technol. (1998).
[64] T. Kanda, V.C. Li, Practical design criteria for saturated pseudo strain hardening behavior in ECC, J. Adv. Concr. Technol. 4(1) (2006) 59-72.
[65] J. Yu, J. Yao, X.Y. Lin, H.D. Li, J.Y.K. Lam, C.K.Y. Leung, I.M.L. Sham, K. Shih, Tensile performance of sustainable Strain-Hardening Cementitious Composites with hybrid PVA and recycled PET fibers, Cem. Concr. Res. 107 (2018) 110-123.
[66] Z.G. Zhang, A. Yuvaraj, J. Di, S.Z. Qian, Matrix design of light weight, high strength, high ductility ECC, Constr. Build. Mater. 210 (2019) 188-197.
[67] H. Ma, Mercury intrusion porosimetry in concrete technology: tips in measurement, pore structure parameter acquisition and application, J. Porous. Mat. 21(2) (2014) 207-215.
[68] S. Diamond, D.N. Winslow, A mercury porosimetry study of the evolution of porosity in Portland cement, J. Mater. 5(3) (1970) 564-585.
[69] Y.W. Zhou, B. Xi, L.L. Sui, S.Y. Zheng, F. Xing, L. Li, Development of high strain-hardening lightweight engineered cementitious composites: Design and performance, Cem. Concr. Compos. 104 (2019) 103370.
[70] O. Onuaguluchi, D.K. Panesar, Hardened properties of concrete mixtures containing pre-coated crumb rubber and silica fume, J. Clean. Prod. 82 (2014) 125-131.
[71] Z.G. Zhang, Q. Zhang, Matrix tailoring of Engineered Cementitious Composites (ECC) with non-oil-coated, low tensile strength PVA fiber, Constr. Build. Mater. 161 (2018) 420-431.
[72] Alibaba for China. https://re.1688.com/, 2021 (accessed 15 May 2021).